

## Mohammad Ali Ansari

Department of Mechanical Engineering, University of Wisconsin-Madison, Madison, WI 53706 e-mail: mansari3@wisc.edu

# **Hemant Agiwal**

Department of Mechanical Engineering, University of Wisconsin-Madison, Madison, WI 53706 e-mail: agiwal@wisc.edu

## **Daniel Franke**

Department of Mechanical Engineering, University of Wisconsin-Madison, Madison, WI 53706 e-mail: dfranke2@wisc.edu

# Michael Zinn

Department of Mechanical Engineering, University of Wisconsin-Madison, Madison, WI 53706 e-mail: mike.zinn@wisc.edu

# Frank E. Pfefferkorn

Department of Mechanical Engineering, University of Wisconsin-Madison, Madison, WI 53706 e-mail: frank.pfefferkorn@wisc.edu

# Shiva Rudraraju'

Department of Mechanical Engineering, University of Wisconsin-Madison, Madison, WI 53706 e-mail: shiva.rudraraju@wisc.edu

# **Numerical Investigation Into the Influence of Alloy Type and** Thermo-Mechanics on Void **Formation in Friction Stir Welding** of Aluminum Alloys

This study employs a high-fidelity numerical framework to determine the plastic material flow patterns and temperature distributions that lead to void formation during friction stir welding (FSW), and to relate the void morphologies to the underlying alloy material properties and process conditions. Three aluminum alloys, viz., 6061-T6, 7075-T6, and 5053-H18, were investigated under varying traverse speeds. The choice of aluminum alloys enables the investigation of a wide range of thermal and mechanical properties. The numerical simulations were validated using experimental observations of void morphologies in these three alloys. Temperatures, plastic strain rates, and material flow patterns are considered. The key results from this study are as follows: (1) the predicted stir zone and void morphology are in good agreement with the experimental observations, (2) the temperature and plastic strain rate maps in the steady-state process conditions show a strong dependency on the alloy type and traverse speeds, (3) the material velocity contours provide a good insight into the material flow in the stir zone for the FSW process conditions that result in voids as well as those that do not result in voids. The numerical model and the ensuing parametric studies presented in this study provide a framework for understanding material flow under different process conditions in aluminum alloys and potentially in other alloys. Furthermore, the utility of the numerical model for making quantitative predictions and investigating different process parameters to reduce void formation is demonstrated. [DOI: 10.1115/1.4062270]

Keywords: aluminum, finite element analysis, predictive model, numerical analysis, voids, material flow, plasticity, bulk deformation processes (e.g. extrusion, forging, wire drawing), machining processes, modeling and simulation

## 1 Introduction

Friction stir welding (FSW) is a solid-state joining process invented by The Welding Institute in the United Kingdom in 1991 [1]. During FSW, a nonconsumable rotating tool penetrates the workpiece and is traversed over a weld seam to produce a joint. High strain rates combined with frictional heating and axial pressure from the tool lead to plastic deformation of the material while maintaining sub-solidus processing temperatures. The plastically deformed material is intermixed around the tool geometry leading to a refined grain structure in the stirred zone [2,3]. The solid-state nature of the process provides FSW significant advantages over conventional fusion-based welding technologies, including the absence of porosity, hot cracks, distortion, and other melting-related defects [4]. The improved microstructure provides the weldment with superior mechanical and corrosion performance over fusion welded parts. FSW also allows for the processing and joining of difficult-to-weld materials such as aluminum and magnesium alloys. With numerous advantages of FSW, the technology faces limitations with respect to large process forces, overhead costs, tool wear, low production rates, and weld geometry restrictions. A schematic of the FSW process is shown in Fig. 1.

The flow of plastically deformed material around the tool probe plays a critical role in the weld quality during FSW. The shearing

action of the tool probe extrudes the plastically deformed material in front of the probe and successively forges the deformed material behind the probe as the tool moves in the welding direction. As is known, process conditions under which FSW is performed significantly affect the weld quality. Some of the process parameters that

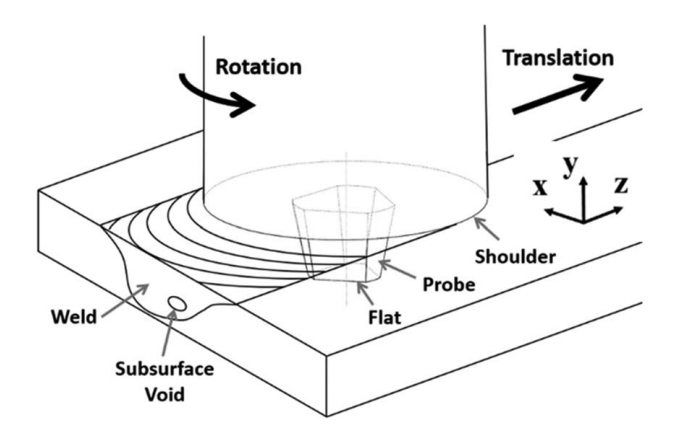


Fig. 1 Schematic of the FSW process. The translational and rotational motion of the tool relative to the workpiece leads to a shearing action on the material by the tool probe. This creates a plastic stir zone that forges the deformed material behind the tool probe. Suboptimal process conditions can potentially lead to defective welds with subsurface voids.

<sup>&</sup>lt;sup>1</sup>Corresponding author.

Manuscript received October 24, 2022; final manuscript received March 31, 2023; published online May 9, 2023. Assoc. Editor: Jingjing Li.

are known to influence the weld quality are the tool traverse and rotational speed [5,6]. In addition, the tilt angle of the tool [7], and the geometry of the probe [8,9] and shoulder [10] influence the temperature distribution around the tool and the resulting material flow [11]. Broadly, there are three types of topological defects caused in the welded specimens in terms of spatial distribution because of insufficient heat flow and/or plastic material flow. When the plastically deformed material is not sufficient to consolidate in the cavity generated by the friction stirring (FS) probe's advance per revolution, it leaves a void behind the trailing edge of the probe. When the processing conditions are such that a void is formed with the probe's every revolution, it leaves a continuous tunnel defect. A void or tunnel defect is limited to the probe-driven region of the weld zone. When the defect extends to the shoulderdriven region and extends all the way to the surface of the weld, it is termed a groove defect [12,13]. Due to the nature of the probe movement, these defects are dominantly seen on the advancing side of the probe. On the contrary, excessive heat input can also produce defective FSW specimens. Considerably high rotational and low traverse speeds can lead to excessive deformation of the material around the tool shoulder. When the tool shoulder is unable to confine this deformed material, the excessive material escapes out as a flash, resulting in thinner stir zones and reduced mechanical properties. Figure 2 shows some of these defect morphologies, as observed in FSW experiments. These cross sections were prepared by authors under different FSW process conditions. The method for sample preparation and cross-sectional observation has been described in Sec. 2. Subsurface defect detection continues to be a foremost challenge during FSW. Post-weld inspections are costly and time consuming. Nondestructive and real-time monitoring techniques for the detection of defects are gathering interest.

In a recent study by the authors of this article, defect formation and material flow during FSW of aluminum 6061 alloys were observed using high-speed high-energy synchrotron X-ray beams [14]. In this first-of-its-kind experimental setup, the author's captured the density changes using high-intensity X-ray beams that showed the periodic formation and filling of the cavity behind the tool probe. Other methods, such as the use of eddy currents [15] and force-based defect monitoring [16,17], have also been implemented successfully. Particularly, attention is drawn to a very recent study by the authors [18] linking some of these defect morphologies with the variations in the reaction force felt by the tool. While in that work, we looked at the interaction of the defect with the tool probe and the reaction forces produced by the tool probe-defect interaction, and in the current article, we look at the material flow and thermo-mechanics aspects. Our aim here is to relate the workpiece temperature distribution and material flow variations of different alloys of a given material (aluminum in this work) to the resulting defect morphologies.

Through recent publications, numerical modeling has proved to be a powerful tool to create a fundamental understanding of the material flow and thermomechanical transformations during FSW and understand defect formation mechanisms. Various numerical frameworks have been proposed in the literature with varying degrees of numerical fidelity (mesh resolution, mesh movement, material flow resolution, time step resolution, etc.) and physics fidelity (thermomechanical material properties and boundary conditions, contact modeling, void representations, etc.). Eulerian (fixed in space) framework-based computational fluid dynamics (CFD) and Lagrangian (attached to the material) framework-based computational solid mechanics are the most-accepted choices for modeling material flow for solid-state processes. However, recent computational studies have focused on combining these two frameworks, yielding the constructs of the coupled Eulerian–Lagrangian (CEL) method and the arbitrary Lagrangian-Eulerian (ALE) method. Schmidt and Hattel [19] simulated the plasticized stir zone and weld voids using the ALE framework. To avoid the high computational cost of the ALE formulations and the incapability of CFD frameworks toward predicting plasticity and void formation, the CEL framework is being widely used in the recent literature and hence is also adopted in this current study. CEL enables better modeling of the material flow, formation of the plasticized stir zone, and different types of voids that might occur during FSW. Some works in the literature that considered the CEL framework are by Al-Badour et al. [20] who used this framework to study the effect of friction and process parameters on the resulting weld and by Zhu et al. [21] who investigated the influence of probe geometry on the material flow around the probe. They showed that the probe feature has a substantial impact on the weld quality. Dialami et al. [22] created a numerical framework based on ALE and CEL stages, and by adding a particle tracing strategy, this framework could simulate defects like joint line remnants. Ajri and Shin [23] have simulated different voids, including cavity, tunnel, groove-like, and excess flash formation, using the CEL framework. Zhu et al. [18] also presented a CEL-based numerical model to simulate defect formation during FSW of 6061-T6 aluminum alloys and understand the effect of processing conditions, tool profile, and defect formation and morphology.

This article is part of a two-part study looking into the interaction of voids with the tool probe and the underlying material flow. The first study, involving void-tool interactions and the novel reaction force signatures observed, which are shown to be useful in remote void detection, has been recently published by the authors [24] in this journal. In this second study, the authors use a similar high-fidelity numerical framework to study the impact of alloy type on material flow and void formation. This study focuses on three different aluminum alloys, viz., Al-6061-T6, Al-5083-H18, and Al-7075-T6, with varying process parameters. As shown in

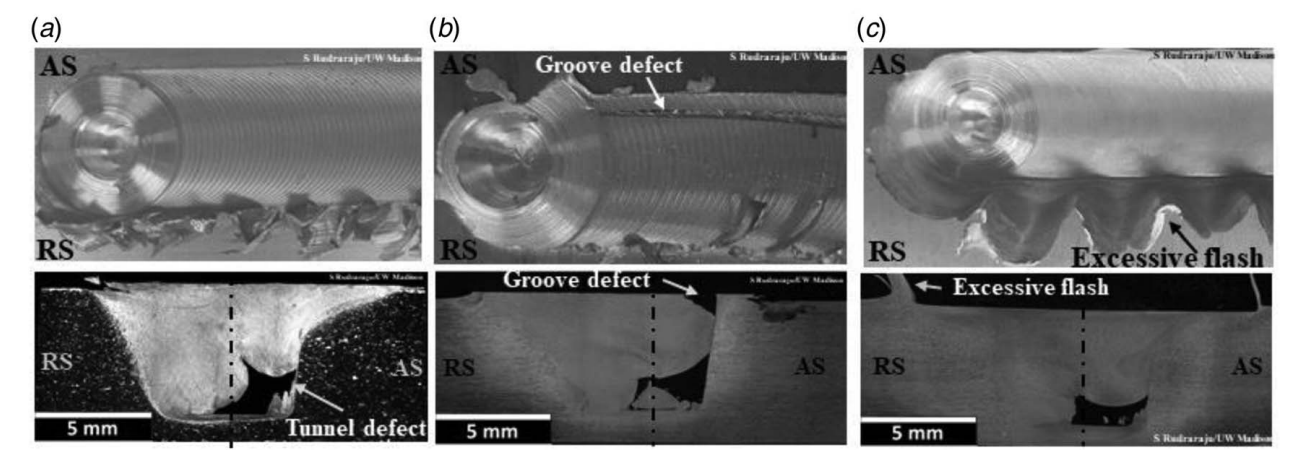


Fig. 2 Top and cross-sectional view image of different defects during FSW (a) tunnel defect, (b) groove-like defect, and (c) excessive flash (AS, advancing side; RS, retreating side)

Table 1 Process parameters for the FSW experiments in this study

Test	Aluminum alloy	Rotational speed (rpm)	Traverse speed (mm/min)
1–3	Al-6061	900	60, 300, 600
4–6	Al-7075		60, 300, 600
7–9	Al-5083		60, 300, 600

this article, variations in the void morphology, temperature distribution, and strain distribution across the three alloys provide significant insights into the effect of temperature-dependent plastic deformation specific to each alloy on their void-forming propensity. The numerical predictions were validated by performing FSW experiments and comparing numerical void morphologies with experimental cross-sectional micrographs of voids. To the author's best knowledge, such a numerical study of the effect of alloy type on void formation has not been sufficiently explored in the literature.

## 2 Experimental Setup

FSW experiments were performed on a three-axis CNC mill (HAAS TM-1) in the position control mode. FSW was performed on three different aluminum alloy workpieces (6061-T6, 7075-T6, and 5083-H18), with all plates of dimensions 200 mm × 100 mm ×6 mm. All experiments were performed using an FS tool made of hardened H13 tool steel, consisting of a 15 mm-diameter concave shoulder and a 5.2 mm-long conical probe tapering from 6.3 mm diameter at the shoulder to 5 mm at the tip. All 120 mm-long FSW tests were performed with a 0 deg travel angle using a 6.35 mm-thick mild steel backing plate. A spindle rotational speed of 900 rpm was used for all experiments, along with a constant plunging speed of 25 mm/min and commanded plunge depth of 0.2 mm. Traverse speeds of 60 mm/min, 300 mm/min, and 600 mm/min were used for producing welds across defective and nondefective regimes. All tests were performed with both the workpiece and tool at room temperature, and multiple repetitions were performed for consistency.

Table 1 lists the experimental parameters needed to create the defective and nondefective welds explored in this study. Process forces during FSW were measured by placing the workpieces atop a three-axis piezo-electric dynamometer (Kistler model 9265). Signals from the dynamometer were guided to the charge amplifiers to read the forces by the DAQ system (National Instruments, BNC-2090A, PCI-6014, PCIe-6320).

The average steady-state forces have been reported and analyzed in this study. Postprocess characterization of welded specimens was performed by cross sectioning the specimens perpendicular to the traverse direction (*X*–*Y*) in the steady-state regimen. The cross sections were ground, polished, and etched to reveal the stir zone. For Al-7075-T6 and Al-5083-H18, Keller's reagent was used, whereas modified Poulton's reagent was used for Al-6061-T6. The prepared cross sections were observed under a white light optical microscopy system (Alicona Infinite Focus).

#### 3 Numerical Framework

We adopt a finite element method (FEM) framework for solving the governing equations of mechanical equilibrium, heat conduction, and contact mechanics that are required in modeling the FSW process. The FSW process and the associated material deformation, thermos-mechanics, and contact mechanics can be effectively treated in a CEL framework of FEM. This framework is available within the ABAQUS Explicit Finite Element package [25].

To reduce the processing time, the proposed numerical model skipped the plunging and dwelling phase, given the slower feed rates of plunge during the FSW process. The volume fraction of the Eulerian domain was defined using a reference domain. The reference domain has empty space with the same probe and shoulder depression geometry at the center, and the rest of the reference domain is the solid material. Since the plunging and dwelling phase of the process was not modeled, the initial startup of the process is nonphysical. To avoid any overestimations due to the nonphysical startup, the numerical results were only investigated when the process's lateral and transitional forces reached a steady-state condition. Further, we consider a constant coefficient of friction during the steady-state condition. This is not a limitation of the numerical model, as the model permits temperaturedependent coefficient of friction values, but we did not have access to the material data of the temperature-dependent coefficient of friction values for the three alloy types considered in this study, and hence, a constant value was considered for each of the alloys. Since the coefficient of friction significantly depends on temperature, to correctly model the heat generated during the FSW process, the corresponding temperature-dependent values of the coefficient of friction should be considered, in general. Our assumption of a constant coefficient of friction is thus one of the potential sources of discrepancy between the numerical results and experimental observations described in this work.

Figure 3(a) shows the Eulerian cube shape domain with a volume of  $25 \times 80 \times 9$  mm<sup>3</sup>. The Eulerian domain included two main regions: The bottom zone (full region) was assigned to the aluminum alloy with a thickness of 6 mm (same as the thickness of the

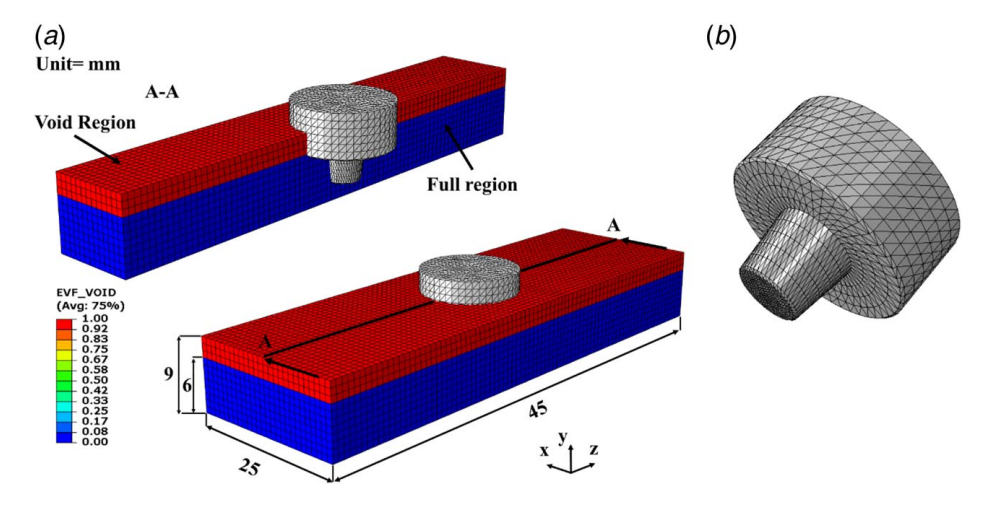


Fig. 3 The geometric domain considered in the CEL framework, showing the problem geometry and the associated numerical discretization (mesh) for (a) the workpiece and (b) the tool

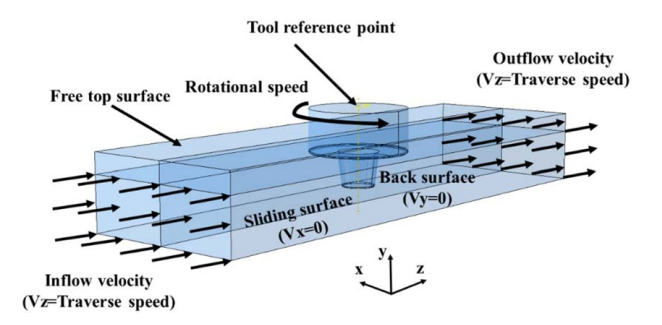


Fig. 4 Boundary conditions enforced on the domain representing the workpiece

experimental plate). In the red zone (void region), no material was assigned, which shows the empty space of the tool at the center and an extra 3 mm empty space at the top of the workpiece into which material can displace (e.g., flash). In a typical example, the Eulerian body is meshed with 24,948 thermally coupled Eulerian elements (EC3D8RT) with a size of 1 mm, having four degrees-of-freedom per node. The meshed FS tool and the tool reference point are presented in Fig. 3(b). The tool is modeled using Lagrangian rigid body formulation consisting of 14,060 four-node thermally coupled tetrahedron (C3D4T) elements with a size of 1 mm. The FS tool dimension and geometry are the same as the tool used in physical experiments.

Because the FS tool was modeled as the rigid Lagrangian body, tool rotational movement and other physical properties (including mass and moment) were assigned to the tool reference point (Fig. 4). The tool movement condition includes rotational speed around its local axis with no other movement along other axes. Because the Eulerian domain is a cube, velocity constraints were assigned to the external surfaces to remove material scape from the bottom and sides of the domain. The welding phase was modeled by the inflow and outflow velocity constraints at the leading edge and trailing edge of the domain. The inflow velocity and outflow velocity were set to the traverse speed of the welding process.

In this framework, we only consider inelastic heat generation by material softening due to model limitations. Therefore, the adiabatic heating is considered, and the heat dissipation into the surroundings is ignored. Also, 95% of the plastic work was assumed to be transformed into thermal energy.

**3.1 Material Model.** Under severe deformation conditions like in FSW, material behavior is highly nonlinear under the large strain, high strain rate, and close-to-solidus temperatures. The Johnson–Cook [26] empirical constitutive law is well known for modeling such strain, strain rate, and temperature regimes in metals. The elasto-plastic evolution of the workpiece material, following the Johnson–Cook material model, is as follows:

$$\sigma_0 = (A + B\bar{\varepsilon}_p^n) \left( 1 + C \ln \frac{\dot{\bar{\varepsilon}}_p}{\dot{\varepsilon}_0} \right) \left( 1 - \left( \frac{T - T_{\text{ref}}}{T_{\text{melt}} - T_{\text{ref}}} \right)^m \right)$$

where  $\bar{\epsilon}_p$ ,  $\dot{\bar{\epsilon}}_p$ , and  $\dot{\epsilon}_0$  are the effective plastic strain rate, and the normalized strain rate, respectively. A, B, C, n, and m are material constants that are measured in a split-Hopkinson bar test, and n, m, and C are constants related to

the effect of strain hardening, thermal softening, and strain rate sensitivity, respectively.  $T_{\rm ref}$  and  $T_{\rm melt}$  are the ambient temperature and the melting point temperature of the material, respectively.

The Johnson–Cook damage model is also used to model the damage evolution during the process. This model accounts for load path dependency by accumulating the damage in local internal variables as the deformation evolves. The scalar damage parameter *D* is given by the following equation.

$$\bar{\varepsilon}_{\rm f} = \left(d_1 + d_2 \exp\left(d_3 \frac{p}{\bar{\sigma}}\right)\right) \left(1 + d_4 \operatorname{Ln}\left(\frac{\dot{\bar{\varepsilon}}_p}{\dot{\varepsilon}_0}\right)\right) (1 + d_5 \bar{\theta}) \text{ and } D = \frac{\bar{\varepsilon}}{\bar{\varepsilon}_{\rm f}}$$

where  $d_1$  to  $d_5$ ,  $p/\bar{\sigma}$ ,  $\bar{\epsilon}$ , and  $\bar{\epsilon}_{\rm f}$  are damage constant, stress triaxiality parameter, accumulative plastic strain, and fracture strain, respectively.

All aluminum alloy properties, including Johnson–Cook model parameters, Johnson–Cook damage model constant, and the thermal and elastic properties of all three alloys, are shown in Tables 2–4, respectively [30–35]. Included are the most important temperature-dependent material properties of all the three alloys modeled in the numerical simulations, including density, thermal diffusivity, heat capacity, and elastic modulus.

To help relate the effect of the temperature-dependent material properties of the three alloys on void-forming mechanisms during FSW, the mechanical strength (ultimate tensile strength (UTS) and yield strength (YS)) of these alloys ranging from room temperature to a high temperature are plotted in Figs. 5(a) and 5(b) [28,36]. Both Al-6061 and 7075 have very close UTS and YS values at a higher temperature, while Al-5083 shows higher UTS and YS values for the 150-300 °C temperature range. This is believed to be due to the differences in the strengthening mechanisms active in the different alloys. Both Aluminum 6061 and Al 7075 are strengthened by precipitation-hardening heat treatment, while Al 5083 is primarily strengthened by strain hardening. Showing the difference in UTS and YS at higher temperatures can demonstrate how different materials flow under the steep gradients of thermal and deformation conditions experienced during the FSW process. It is important to note that obtaining such extensive material data for temperature-dependent material properties requires collecting experimental data from varied sources in the literature, and hence, there are some gaps in the temperature ranges for some of these alloys.

# 4 Results and Discussion

**4.1 Numerical Model Validation.** The results from the numerical model were compared with the experimental observations of weld surface appearance, void cross-sectional morphology, and steady-state process forces. To compare the weld morphology for subsurface defects and material flow patterns two traverse cross sections were considered and tracked in the experimental and numerical specimens. Cross-section "A-A" (Fig. 6) was created behind the trailing edge of the tool to visualize the void morphology, and cross-section "B-B" (Fig. 6) was created at the trailing edge of the tool beneath the shoulder to visualize the material flow. Both cross sections were taken in the steady-state regimen of the weld.

Due to system compliance, the actual plunge reduces compared to the commanded plunge in the experiments. The maximum

Table 2 Johnson-Cook plasticity model constants

Material	A (MPa)	B (MPa)	C	n	m	$T_{\text{ref}}$ (°C)	T <sub>melt</sub> (°C)
Al 6061-T6 [27]	324	114	0.002	0.42	1.34	25	652
Al 7075-T6 [28]	546	678	0.059	0.72	1.56	25	635
Al 5083-H18 [29]	170	425	0.0335	0.42	1.225	25	640

Table 3 Johnson-Cook damage constants

Material	$d_1$	$d_2$	$d_3$	$d_4$	$d_5$	$\dot{\boldsymbol{arepsilon}}_0$	$T_{\text{Transition}}$ (°C)	T <sub>melt</sub> (°C)
Al 6061-T6 [30]	-0.068	0.451	-0.952	0.036	0.697	1	25	652
Al 7075-T6 [31]	-0.068	0.451	-0.952	0.036	0.697	1	25	635
Al 5083-H18 [32]	0.0261	0.263	-0.349	0.147	16.8	1	25	640

Table 4 Temperature-dependent material properties for the three alloys

Al 6061-T6 [33]								
Temperature (°C)	Thermal conductivity (W/m °C)	Specific heat (J/kg °C)	Density (kg/m <sup>3</sup> )	Thermal expansion (10 <sup>-6</sup> /°C)	Young's modulus (GPa)	Poisson's ratio		
25	162	945	2690	23.5	66.94	0.33		
100	177	978	2690	24.6	63.21	0.334		
149	184	1000	2670	25.7	61.32	0.335		
204	192	1030	2660	26.6	56.8	0.336		
260	201	1052	2660	27.6	51.15	0.338		
316	207	1080	2630	28.5	47.17	0.36		
371	217	1100	2630	29.6	43.51	0.4		
427	229	1130	2600	30.7	28.77	0.41		
482	243	1276	_	_	20.2	0.42		

Al 7075-T6 [34]

Temperature (°C)	Thermal conductivity (W/m °C)	Specific heat (J/kg °C)	Density (kg/m <sup>3</sup> )	Thermal expansion $(10^{-6})^{\circ}$ C)	Young's modulus (GPa)
25	131	750	2810	21.8	72.4
76.85	133	750	2750	22.3	71
126.85	140	840	2684	22.8	68.1
176.85	145	960	2612	23.4	63.9
226.85	152	1000	2577	24.1	58.2
276.85	157	1040	2520	24.7	49
326.85	164	1087	2457	25.2	35
376.85	169	1129	2425	25.7	20.5
426.85	176	1171	2356	26.3	16.9

Al 5083 [32,33]

Temperature (°C)	Thermal conductivity (W/m °C)	Specific heat (J/kg °C)	Density (kg/m <sup>3</sup> )	Temperature (°C)	Thermal expansion (10 <sup>-6</sup> /°C)	Temperature (°C)	Young's modulus (GPa)
25	117	924	2660	25	_	25	70
80	122.7	984.2	2640	200	25.5	100	67.8
180	131.6	1039.6	2630	300	26.8	200	60.7
280	142.3	1081.2	2610	400	28.9	250	43.1
380	152.5	1136.6	2590	500	31.5	300	42
480	159.5	1178.2	2570			350	36
580	177.2	1261.4	2550			400	26.8
_	_	_	_	_	_	450	19.4
_	_	_	_	_	_	500	14.9

resemblance in the actual and commanded plunge was found when the traverse speed was lowest (60 mm/min). For this processing condition, the average steady-state forces for both experimental and numerical setups across the three alloys have been compared (Table 5). The steady-state forces are within 10% error for all three alloys, suggesting strong agreement between the experiments and numerical simulations. Forces were highest for 7075-T6, followed by 5083-H18, and lowest for 6061-T6 alloy. The variation can be attributed to the different hardness of these materials, with 7075-T6 having the highest hardness and 6061-T6 being the lowest.

The weld morphology from the experimental and numerical simulation setups has been compared in Fig. 7. Figure 7(i and ii) compares the top view of the coating. There is coherence in the flash formation seen around the weld path for both setups. The flash is excessively produced on the retreating side of the weld

for all alloys. The flash formation is highest for 6061-T6, followed by 7075-T6 and 5083-H18, in that order. The extent of flash formation can be attributed to the high-temperature strength of each alloy, with 5083-H18 having the highest high-temperature mechanical properties (Fig. 5). The morphologies compared in this figure are for the traverse speed of 600 mm/min. At this condition, voids were produced in all the alloys. The continuous tunnel defect in all alloys can be observed in the side view of the simulation (Fig. 7(iii)). These defects are observed in much depth by looking at the traverse cross section (A-A) for both numerical and experimental setups in Fig. 7(iv and v), respectively. The tunnel defect morphology is comparable in both experimental and numerical results. The size of the tunnel defect is larger in the 6061-T6 alloy compared to the 7075-T6 alloy. In the 5083-H18 alloy, the tunnel defect extended to the shoulder of the FS probe and grove

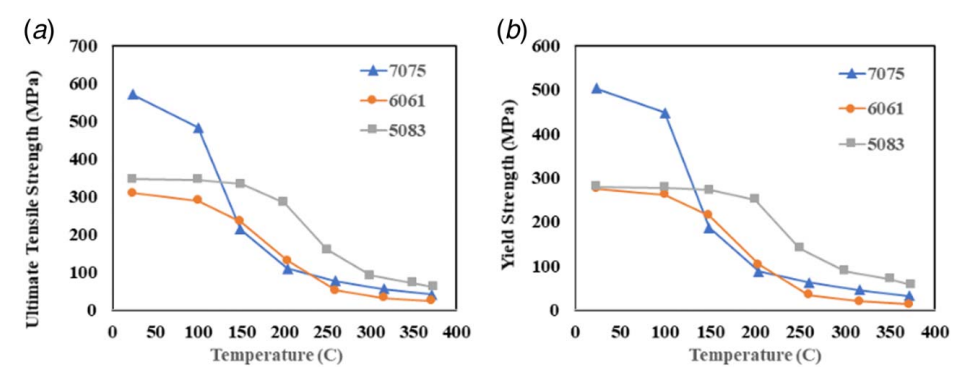


Fig. 5 Temperature-dependent material properties of three aluminum alloys: (a) ultimate tensile strength (MPa) and (b) yield strength (MPa) [28,36]

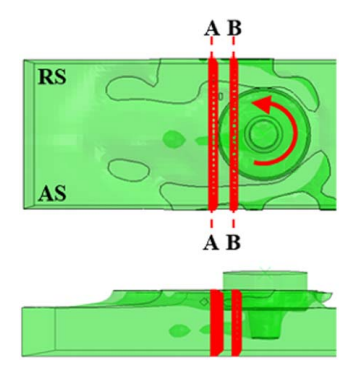


Fig. 6 Workpiece cross sections considered in the numerical model to observe process dynamics

is observed. For 6061-T6 and 5083-H18 alloys, the defects were dominantly situated on the advancing side of the stir zone, whereas for the 7075-T6 alloys, the void was much closer to the center of the stir zone.

**4.2 Effect of Processing Parameters on Material Flow and Defect Formation.** During the FSW process for a well-consolidated bond, the processing conditions should allow for the sufficient plastic material flow of the material around the tool probe. The authors have shown in a recent study that during a rotation of the FS tool probe, a cavity is formed behind the probe, which is then filled by the forging of the plastic material flow. Optimum friction surfacing conditions allow for processing temperatures of 70–90% of the solidus temperature of the workpiece material. For aluminum alloys within this temperature range, solution treatment takes place and affects the malleability of the material and leads to material softening and ease of flow [3]. Each aluminum alloy has a different as-cast property and transforms accordingly for a given processing condition. Thus, weld consolidation becomes a strong function of the process parameters and the alloy type.

For all three alloys in the study, three combinations of traverse and rotation speed were studied (Table 1). The cross-sectional macrographs from experiments and numerical simulation are

shown in Fig. 8. The numerical simulations are in strong coherence with the experimental results with respect to void location and morphology, except for experiments done at 60 mm/min. In the numerical simulations, fully consolidated welds without any subsurface voids are created at 60 mm/min traverse speed for all alloys, whereas at 300 mm/min and 600 mm/min, we start observing voids. At 60 mm/min traverse speed, in contrast to the simulated result, the void morphology is significantly different in the experiments. The discrepancies may have been caused by the numerical framework assumptions such as an absence of dynamics from the machine and tool holder (runout), the eccentricity of the tool, rigid Lagrangian body formulation for the tool, adiabatic heat effect, and constant friction coefficient. It seems like the effect of these assumptions is more prominent at lower traverse speeds. These limitations of the numerical model will be highlighted later in the discussion. The void size increases with the traverse speed since, for the given rotation speed, the process is getting colder and the consolidation time for the plastically deformed material, along with the overall heat generation, reduces. As mentioned in the above section, groove defects were observed in the 5083-H18 alloy, whereas tunnel defect was observed in the other cases.

To understand these variations in defect morphology with alloy and traverse speeds, the workpiece temperature distributions across the nine processing conditions are extracted from the numerical simulations and shown in Fig. 9. Some general trends observed across all conditions include higher temperatures around the tool shoulder compared to the probe, a phenomenon well reported in the literature. Asymmetry in the distribution of temperature in the stir zone exists, with the advancing side cooler than the retreating side. The temperature variance can be attributed to the extrusion cycle of the plastically deformed material, which flows toward the advancing side from the retreating side [37]. As mentioned earlier, increasing the traverse speed leads to colder welds, and the reduction in temperature in the stir zone is visible for all three alloys.

Along with temperature, the strain rate plays a crucial role in plastic deformation. The equivalent plastic strain has been demonstrated from the numerical simulations in Fig. 10. The observed strain rates are of the order  $10^3$ – $10^4$  s<sup>-1</sup>, and these values are consistent with the literature [27,29]. Strain rates generated during FSW are dependent on the tangential velocity of the tool and the shearing capability of the tool design. The introduction of features

Table 5 Experimental and numerical steady-state axial force during the stirring phase

Aluminum	Traverse speed (mm/min)	Rotational speed (rpm)	Average experimental steady-state force (N)	Average numerical steady-state force (N)	Error (%)
6061-T6	60	900	4364	4270	2.1
7075-T6			8148	7490	8.1
5083-H18			7230	6870	5.0

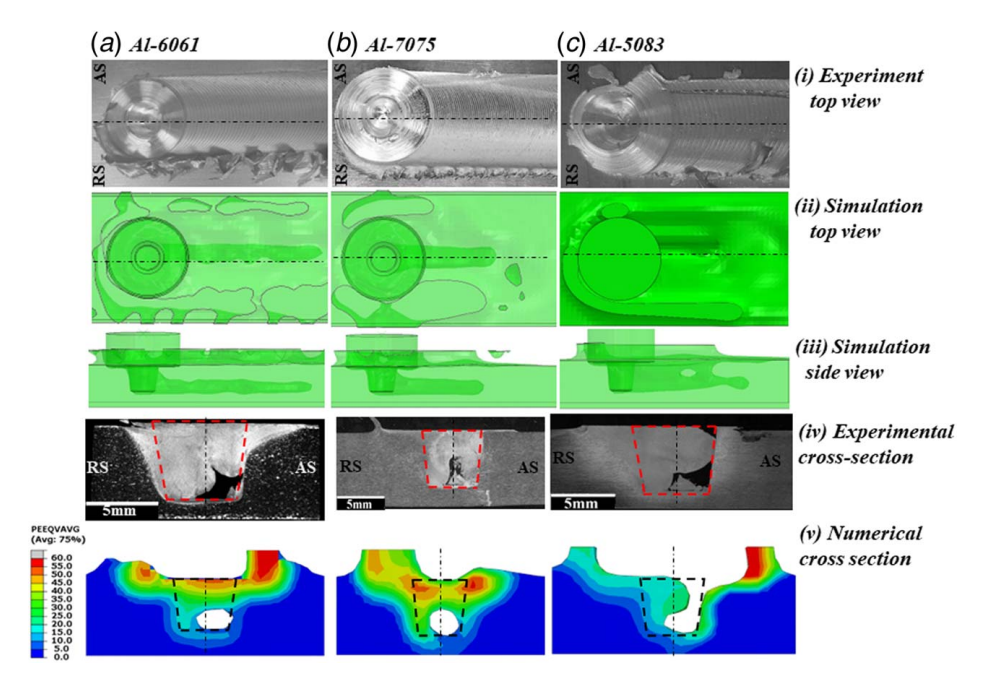


Fig. 7 Comparison between experimental and numerical results for a traverse speed of 600 mm/min for (a) aluminum 6061-T6, (b) aluminum 7075-T6, and (c) aluminum 5083-H18

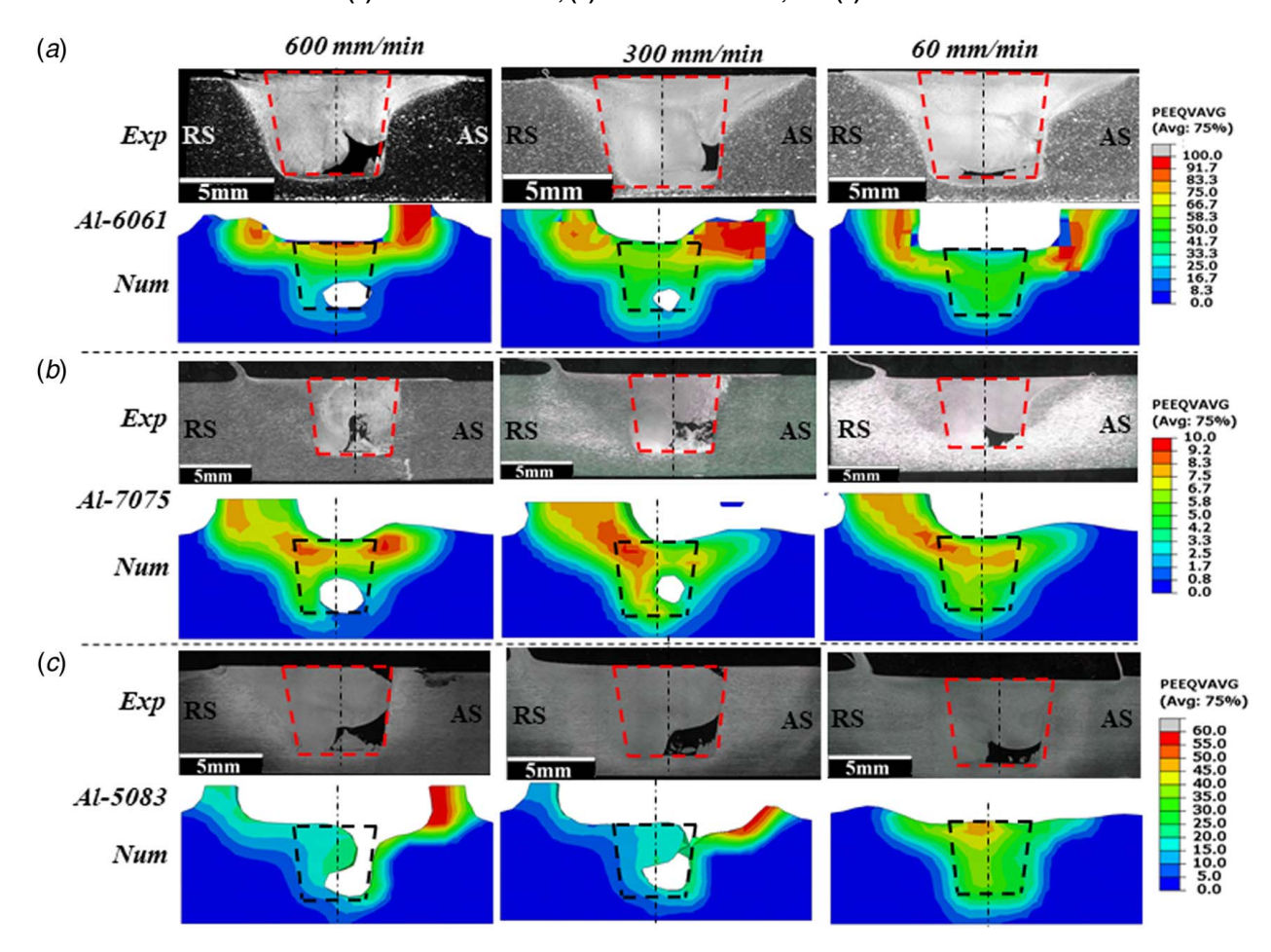


Fig. 8 Void morphology observed in the numerical and experimental cross sections at three traverse speeds for (a) Al-6061-T6, (b) Al-7075-T6, and (c) Al-5083-H18

such as threads and flats improves the effective shearing of the surrounding material. Since, in this study, the tool has no additional features and the rotational speed of the tool is constant across all experiments, the effective strain rate is dependent on the traverse speed and alloy type. Literature has found the strain rate to be inversely proportional to the weld pitch (advance of tool per revolution). The strain rates were found to increase slightly near the tool—workpiece interface for the 6061-T6 and the 7075-T6 alloys,

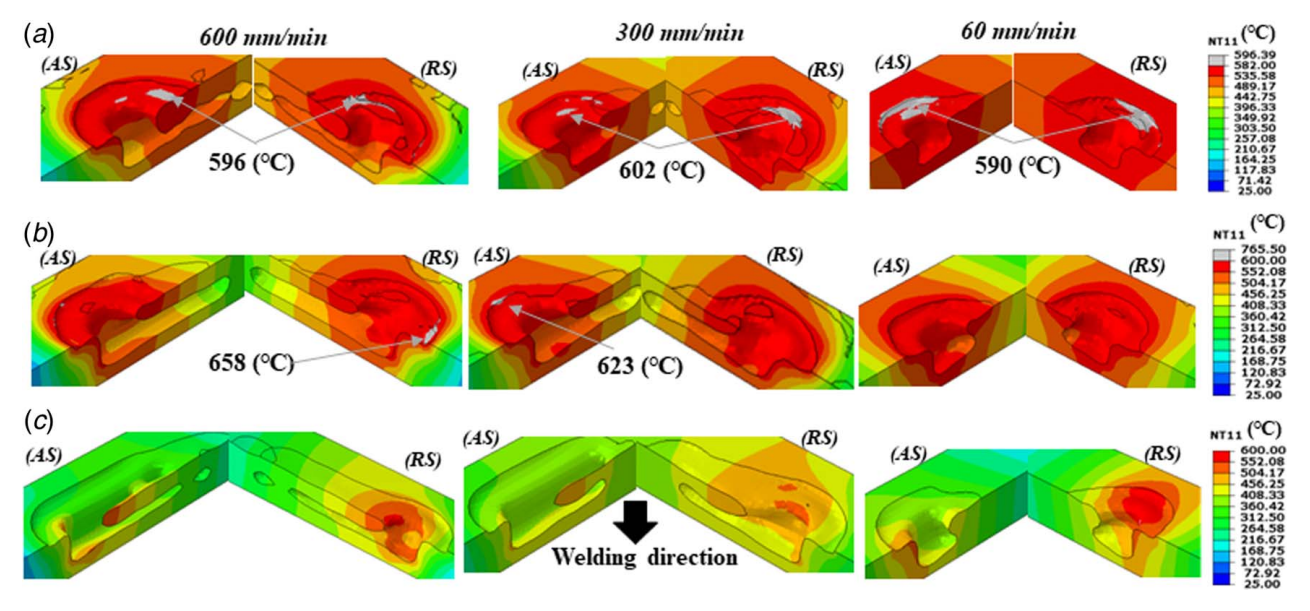


Fig. 9 Temperature distribution around the tool and probe at three traverse speeds for (a) Al-6061-T6, (b) Al-7075-T6, and (c) Al-5083-H18

with the increasing traverse speed. Within the stir zone, the strain rate variation is similar to the temperature variation. Lower strain rates in the stir zone with higher traverse speed and higher strain rates on the retreating side were observed for both alloys. This can be potentially attributed to the increased weld pitch or the advance of the FS tool per revolution. An increased weld pitch leads to an increase in the stirred material per revolution, which can reduce the strain rates. The combined effect of strain rate and temperature drives the plastic flow during FSW. Around the probe region, a reduction in temperature and strain rates was observed, which can be correlated with the increased void size.

**4.3** Effect of Alloy Type on Material Flow and Defect Formation. Comparing the three alloys for a given traverse speed, we have seen the variance in void morphology in Fig. 7. The three alloys vary in their chemical composition and thermomechanical properties. Re-summarizing the material properties reported earlier, 6061-T6 has the highest thermal conductivity and specific heat, followed by 5083-H18 and 7075-T6. At room temperature, 7075-T6 has the highest tensile and yield strength, whereas 5083-H18 has a considerably higher elevated temperature tensile and yield strength compared to the other two alloys.

For 6061-T6 FSW specimens, the average temperature under the shoulder is close to 570 °C and ranges from 400 °C-550 °C around the probe, depending on the traverse speed (Fig. 9). The least temperatures can be observed corresponding to the void locations in the stir zone. There are a few spots close to the shoulder where the temperature exceeds the solidus (582 °C), and localized melting is observed. The other two alloys, 7075-T6 and 5083-H18, also show similar variations. In the case of 7075-T6, the temperature is above the solidus temperature of 477 °C, and this has also been reported in other experimental studies [38]. 5083-H18 alloy, which has a similar solidus temperature to 6061-T6 (580 °C), has lower temperatures in the stir zone compared to the latter, which can be attributed to the higher tensile properties at elevated temperatures. The strain rate maps in Fig. 10 show the 7075-T6 alloy to be the most highly strained compared to the other two alloys. Since the thermal conductivity and heat capacity of the 7075-T6 alloy is the lowest, it can convert a higher amount of that heat generation into the plastic flow and increased shearing of the surrounding material. The higher hot strength of the 5053-H18 alloy leads to the lowest strain rates and temperature profiles around the tool probe and the shoulder. This results in the void extending to the tool-workpiece interface and thus forming a groove defect.

Due to the tool geometry, thermal boundary conditions, and asymmetric plastic strain, the material flow in the stir zone during FSW is complex. Fratini et al. [39] demonstrated the complex flow lines within the stir zone for conditions with and without voids. The flow directions indicate material transferring from the retreating side toward the advancing side of the workpiece. The material underneath the shoulder moves in bulk streams (shoulderdriven flow). As the tool was tilted 2 deg, a slight vertical material flow was observed on the retreating side. Then it changes the direction, moving upward to make the ascending laminar flow on the advancing side. Swirl phenomena at the bottom of the weld were observed, indicating an ineffective material flow and signs of internal tunnel defects due to the material discontinuities [39]. In contrast, the material flow at the transverse cross section of the nondefected weld (shown in the study by Fratini et al. [39]) is more homogenous with a circular pattern between the advancing side and retreating side, and with no swirl phenomena at the edges.

The material flow was similarly visualized in this work by observing the material velocity vectors (enabled in the ABAQUS CEL framework) along with the underlying temperature distribution in the transverse cross sections of the FSW specimens from numerical simulations (Fig. 11). The velocity vectors are shown for the "B-B" cross section mentioned earlier in Fig. 6. This cross section is taken within the stir zone, right underneath the interface of the FS tool and shoulder. Figure 11(a) represents a fully consolidated weld achieved at a traverse speed of 60 mm/min for the 6061-T6 alloy. The velocity vectors follow similar trends to flow vectors shown in Fig. 11(b). As mentioned earlier, the material underneath the shoulder achieves the maximum temperature close to the solidus, and the overall temperature in the stir zone is nearly constant. The velocity vectors show the flow from the retreating side to the advancing side, with material pushed down on the retreating and moving upward on the advancing side. The circular flow pattern is not observed in the simulations, possibly because of the 0 deg tool tilt, no eccentricity, runout, and the absence of tool features.

For the traverse speed of 600 mm/min, at which tunnel defects are seen in the stir zone, the velocity flow patterns are in strong agreement with Fig. 11(a). The flow pattern near the shoulder is similar to the consolidated weld case; however, in the probe, there are stark differences. Smaller velocity vectors are observed around the void, suggesting the absence of flow, and the swirl phenomena, as observed in microstructural observations, are also seen near the bottom of the advancing side. Comparing the same processing condition in the 5053-H18 alloy, which has a groove defect, the

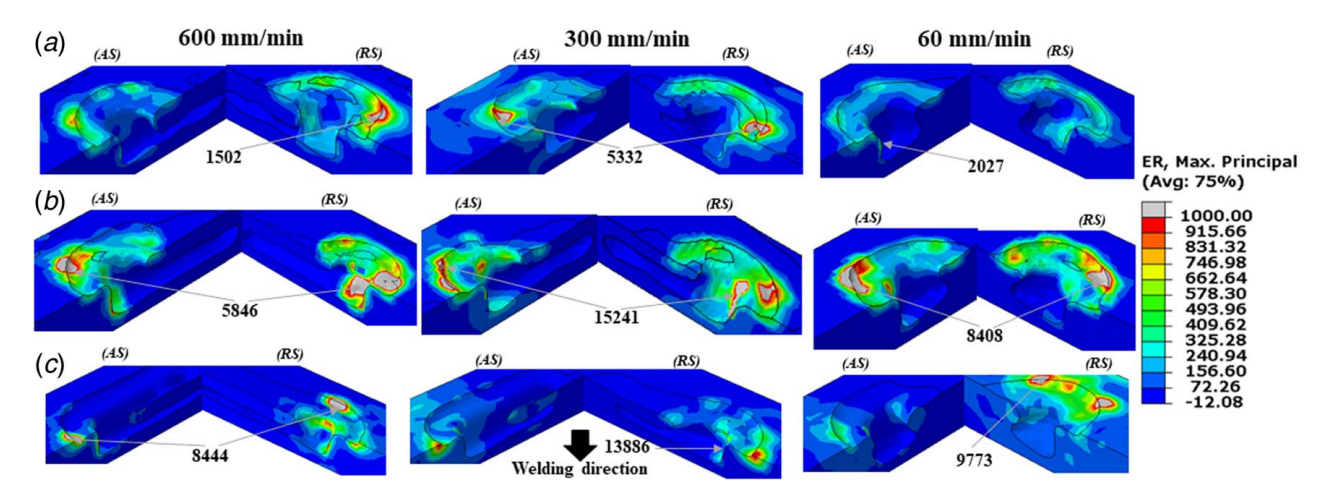


Fig. 10 Plastic strain rate around the tool and probe at three traverse speeds for (a) Al-6061-T6, (b) Al-7075-T6, and (c) Al-5083-H18

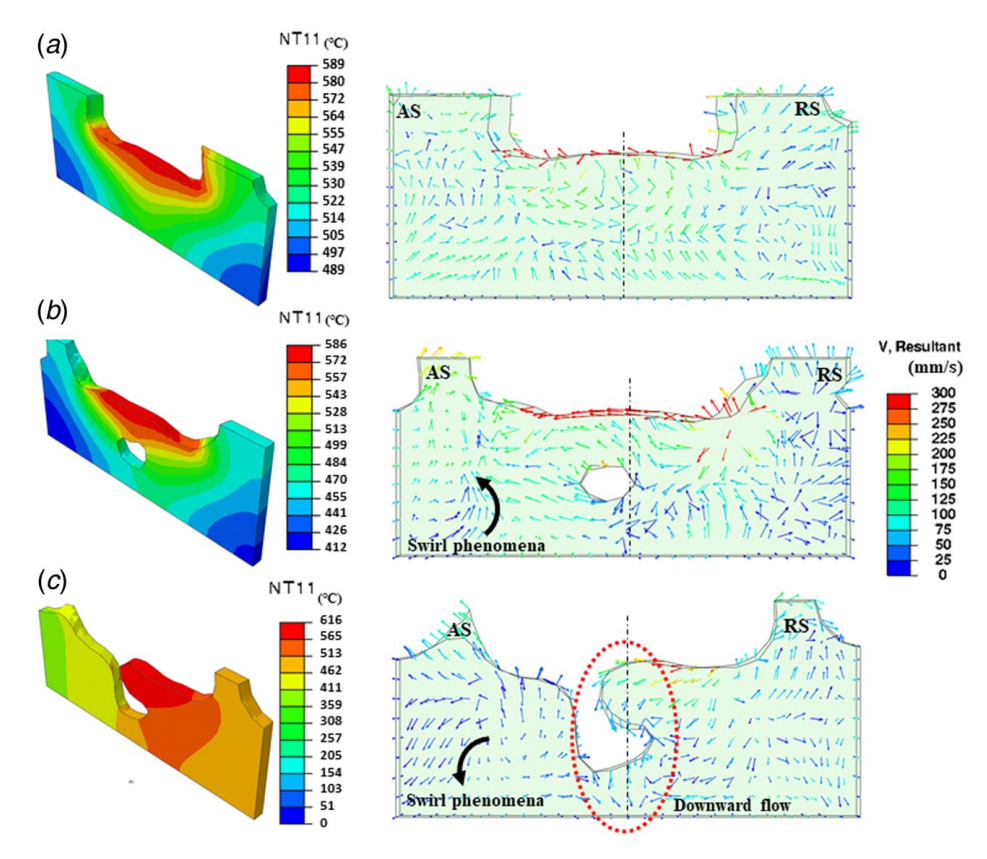


Fig. 11 Temperature distribution and material velocity vectors at a transverse cross section for (a) Al-6061-T6 at 60 mm/min traverse speed, (b) Al-6061-T6 at 600 mm/min traverse speed, and (c) Al-5083-H18 at 600 mm/min traverse speed

swirl phenomenon is also seen at the bottom of the advancing side. The velocity vectors have smaller magnitudes compared to 6061-T6 alloys, suggesting reduced plastic flow that was also observed through the reduced temperatures and plastic strain rates earlier.

#### 5 Conclusion

This study employs a coupled Eulerian–Lagrangian FEM framework to obtain the temperature distribution and the resulting plastic flow underlying void formation during the FSW process. Three aluminum alloys were investigated for void formation and morphology under varying process parameters, and the numerical predictions from the simulations were validated by comparing them with

corresponding experimental observations. The focus is on correlating the underlying temperature distribution, plastic strain rate, and material flow patterns with the void morphology. The key results and observations from this study are summarized as follows:

- (a) The stir zone and void morphology were in good agreement with the experimental observations. The numerical model can predict void location and size with considerable confidence. For process parameters in the defective regime, tunnel defects were observed for the 6061-T6 and 7075-T6 alloys, whereas the 5053-H18 alloy showed a groove defect.
- (b) The plastic strain rate and temperature distributions in the steady-state regimen were recorded, and these show a

strong dependence on the traverse speed and the alloy type. Both temperature and strain rates were higher in the shoulder-driven zone of the stir zone compared to the probedriven material. The retreating side of the weld showed a higher temperature and strain rate compared to the advancing side.

- (c) Due to the higher tensile properties at elevated temperatures for the 5053-H18 alloy, the plastic strain rates and temperatures were least compared to others. Lower thermal conductivity and specific heat of 7075-T6 alloys led to increased shearing (plastic flow) in the stir zone.
- (d) The material velocity vectors provided insights into the material deformation in the stir zone for both defect and nondefect regimens. When voids are formed, a swirl phenomenon was observed on the advancing side of the probe, with a low magnitude of velocity vectors around the void. Due to the higher elevated tensile properties of the 5053-H18 alloy, the velocity vectors had the least magnitude.

The numerical framework presented here is shown to be useful for predicting different types of defects in aluminum alloys, and is potentially extendable to other FSW alloys. The utility of the numerical framework for investigating different process parameters and process variables to reduce void formation and to make related quantitative predictions has been demonstrated. However, many standard assumptions and simplifications intrinsic to the numerical model, with respect to the boundary conditions, material properties, material model, space-time discretization, etc., need to be accounted for when comparing with experimental observations. The model presented here does not consider the compliance of the machine, runout, and eccentricity of the tool. However, these three effects were studied in a recent publication by the authors [24]. It also assumes a rigid tool body and an adiabatic heat condition. As a result, the plunge depth remains consistent in the numerical model, which is not the case in the experiments. Further, in the current model, we did not explicitly track the division of the generated heat energy between the workpiece and the tool. Since the temperature continuity is ensured by the continuity of the temperature primal field in the FEM computations across the tool and workpiece, one can expect the heat energy to be distributed in proportion to the thermal conductivities of the tool and workpiece, respectively, but this has not been explicitly enforced and will be more carefully considered in our future studies. Further, under some process conditions, the numerical model overpredicts the process forces, and there are some inconsistencies in the void morphology: The model does not predict voids at 60 mm/min, which was seen in the experiments, and overpredicts the size of voids for 300 mm/min and 600 mm/min compared to the experiments.

As mentioned earlier, the numerical studies and the process signatures (temperature distribution, strain distribution, material flow, and void morphology) studied in this article are complementary to a recent publication by the authors in this journal [24], which correlated the process force signals with defect formation and void morphologies. Moving forward, the machine compliance, tool features, tool eccentricity, and runout will be implemented in this numerical framework to make the model more coherent with the experiments.

# Acknowledgment

The support of colleagues in the Multiscale Metal Manufacturing Processes Lab and the Department of Mechanical Engineering at the University of Wisconsin-Madison is gratefully acknowledged.

# **Funding Data**

 The U.S. National Science Foundation (NSF Grant No. CMMI-1826104).

# **Conflict of Interest**

There are no conflicts of interest.

#### **Data Availability Statement**

The authors attest that all data for this study are included in the paper.

#### References

- Thomas, W. M., Nicholas, E. D., Needham, J. C., Murch, M. G., Temple-Smith, P., and Dawes, C. J., 1995, "Friction Welding," U.S. Patent 5,460,317.
- [2] Leal, R. M., and Loureiro, A., 2004, "Defects Formation in Friction Stir Welding of Aluminium Alloys" Materials Science Forum, 455, pp. 299–302.
- [3] Mishra, R. S., and Ma, Z. Y., 2005, "Friction Stir Welding and Processing," Mater. Sci. Eng., R, 50(1–2), pp. 1–78.
- [4] Yoshikawa, K., 2003, "A Joining Criterion for Lap Joining of Dissimilar Metal Materials of Aluminum and Stainless Steel by Friction Stir," The 4th International Symposium on Friction Stir Welding, Park City, UT.
- [5] Kim, Y. G., Fujii, H., Tsumura, T., Komazaki, T., and Nakata, K., 2006, "Effect of Welding Parameters on Microstructure in the Stir Zone of FSW Joints of Aluminum Die Casting Alloy," Mater. Lett., 60(29–30), pp. 3830–3837.
- [6] Ren, S. R., Ma, Z. Y., and Chen, L. Q., 2007, "Effect of Welding Parameters on Tensile Properties and Fracture Behavior of Friction Stir Welded Al–Mg–Si Alloy," Scr. Mater., 56(1), pp. 69–72.
- [7] Morisada, Y., Imaizumi, T., and Fujii, H., 2015, "Clarification of Material Flow and Defect Formation During Friction Stir Welding," Sci. Technol. Weld. Join., 20(2), pp. 130–137.
- [8] Chen, G., Li, H., Wang, G., Guo, Z., Zhang, S., Dai, Q., Wang, X., Zhang, G., and Shi, Q., 2018, "Effects of Pin Thread on the In-Process Material Flow Behavior During Friction Stir Welding: A Computational Fluid Dynamics Study," Int. J. Mach. Tools Manuf., 124(1), pp. 12–21.
- [9] Su, H., Wu, C. S., Bachmann, M., and Rethmeier, M., 2015, "Numerical Modeling for the Effect of Pin Profiles on Thermal and Material Flow Characteristics in Friction Stir Welding," Mater. Des., 77(1), pp. 114–125.
- [10] Padmanaban, G., and Balasubramanian, V., 2009, "Selection of FSW Tool Pin Profile, Shoulder Diameter and Material for Joining AZ31B Magnesium Alloy —An Experimental Approach," Mater. Des., 30(7), pp. 2647–2656.
- [11] Rasti, J., 2018, "Study of the Welding Parameters Effect on the Tunnel Void Area During Friction Stir Welding of 1060 Aluminum Alloy," Int. J. Adv. Manuf. Technol., 97(5–8), pp. 2221–2230.
- [12] Kim, Y. G., Fujii, H., Tsumura, T., Komazaki, T., and Nakata, K., 2006, "Three Defect Types in Friction Stir Welding of Aluminum Die Casting Alloy," Mater. Sci. Eng. A, 415(1-2), pp. 250-254.
- [13] Arbegast, W. J., Coletta, E. R., and Li, Z., 2001, "Characterization of Friction Stir Weld Defect Types," TMS 2001 Annual Spring Meeting, New Orleans, LA, Feb. 11, pp. 11–15.
- [14] Agiwal, H., Ansari, M. A., Franke, D., Faue, P., Clark, S. J., Fezzaa, K., Rudraraju, S., Zinn, M., and Pfefferkorn, F. E., 2022, "Material Flow Visualization During Friction Stir Welding Using High-Speed X-Ray Imaging," Manuf. Lett., 34(1), pp. 62–66.
- [15] Rosado, L. S., Santos, T. G., Piedade, M., Ramos, P. M., and Vilaça, P., 2010, "Advanced Technique for Non-Destructive Testing of Friction Stir Welding of Metals," Measurement, 43(8), pp. 1021–1030.
- [16] Boldsaikhan, E., Corwin, E. M., Logar, A. M., and Arbegast, W. J., 2011, "The Use of Neural Network and Discrete Fourier Transform for Real-Time Evaluation of Friction Stir Welding," Appl. Soft Comput., 11(8), pp. 4839–4846.
- [17] Shrivastava, A., Pfefferkorn, F. E., Duffie, N. A., Ferrier, N. J., Smith, C. B., Malukhin, K., and Zinn, M., 2015, "Physics-Based Process Model Approach for Detecting Discontinuity During Friction Stir Welding," Int. J. Adv. Manuf. Technol., 79(1), pp. 605–614.
- [18] Zhu, Z., Wang, M., Zhang, H., Zhang, X., Yu, T., and Wu, Z., 2017, "A Finite Element Model to Simulate Defect Formation During Friction Stir Welding," Metals, 7(7), p. 256.
- [19] Schmidt, H., and Hattel, J., 2004, "A Local Model for the Thermomechanical Conditions in Friction Stir Welding," Modell. Simul. Mater. Sci. Eng., 13(1), pp. 77–93.
- [20] Al-Badour, F., Merah, N., Shuaib, A., and Bazoune, A., 2013, "Coupled Eulerian Lagrangian Finite Element Modeling of Friction Stir Welding Processes," J. Mater. Process. Technol., 213(8), pp. 1433–1439.
- [21] Zhu, Y., Chen, G., Chen, Q., Zhang, G., and Shi, Q., 2016, "Simulation of Material Plastic Flow Driven by Non-Uniform Friction Force During Friction Stir Welding and Related Defect Prediction," Mater. Des., 108(1), pp. 400–410.
- [22] Dialami, N., Cervera, M., Chiumenti, M., and Segatori, A., 2019, "Prediction of Joint Line Remnant Defect in Friction Stir Welding," Int. J. Mech. Sci., 151(1), pp. 61–69.
- [23] Ajri, A., and Shin, Y. C., 2017, "Investigation on the Effects of Process Parameters on Defect Formation in Friction Stir Welded Samples via Predictive Numerical Modeling and Experiments," ASME J. Manuf. Sci. Eng., 139(11), p. 111009.
- [24] Ansari, M. A., Agiwal, H., Zinn, M., Pfefferkorn, F., and Rudraraju, S., 2022, "Novel Correlations Between Process Forces and Void Morphology for

- Effective Detection and Minimization of Voids During Friction Stir Welding," ASME J. Manuf. Sci. Eng., 144(9), p. 091007.
- [25] Fratini, L., Buffa, G., Palmeri, D., Hua, J., and Shivpuri, R., 2006, "Material Flow in FSW of AA7075-T6 Butt Joints: Continuous Dynamic Recrystallization Phenomena," J. Eng. Mater. Technol., 128(3), pp. 428–435.
- [26] Johnson, G. R., and Cook, W. H., 1983, "A Constitutive Model and Data for Metals Subjected to Large Strains, High Strain Rates and High Temperatures," Proceedings of the 7th International Symposium on Ballistics, Vol. 21, No. 1, pp. 541–547.
- [27] Ansari, M. A., Samanta, A., Behnagh, R. A., and Ding, H., 2019, "An Efficient Coupled Eulerian-Lagrangian Finite Element Model for Friction Stir Processing," Int. J. Adv. Manuf. Technol., 101(5–8), pp. 1495–1508.
- [28] MatWeb, 2018, "Material Property Data: Aluminum 3003-O, Aluminum 6061-T6; 6061-T651, Aluminum 7075-T6; 7075-T651, Aluminum 2024-T3," www. matweb.com
- [29] Pan, W., Li, D., Tartakovsky, A. M., Ahzi, S., Khraisheh, M., and Khaleel, M., 2013, "A New Smoothed Particle Hydrodynamics Non-Newtonian Model for Friction Stir Welding: Process Modeling and Simulation of Microstructure Evolution in a Magnesium Alloy," Int. J. Plast., 48(1), pp. 189–204.
- [30] HI, G. G., Chen, S. R., Wright, W., and Lopez, M. F., 1994/Los Alamos National Laboratory Report: LA-12669-MS, Constitutive Equations for Annealed Metals Under Compression at High Strain Rates and High Temperatures.
- [31] Soundararajan, V., Zekovic, S., and Kovacevic, R., 2005, "Thermo-Mechanical Model With Adaptive Boundary Conditions for Friction Stir Welding of Al 6061," Int. J. Mach. Tools Manuf., 45(14), pp. 1577–1587.

- [32] Kim, D., Badarinarayan, H., Kim, J. H., Kim, C., Okamoto, K., Wagoner, R. H., and Chung, K., 2010, "Numerical Simulation of Friction Stir Butt Welding Process for AA5083-H18 Sheets," Eur. J. Mech. A/Solids, 29(2), pp. 204–215.
- [33] Jamshidi, A. H., Serajzadeh, S., and Kokabi, A. H., 2011, "Evolution of Microstructures and Mechanical Properties in Similar and Dissimilar Friction Stir Welding of AA5086 and AA6061," Mater. Sci. Eng. A, 528(28), pp. 8071–8083.
- [34] Narender, K., Madhusudhan Rao, A. S., Gopal Kishan Rao, K., and Gopi Krishna, N., 2013, "Temperature Dependence of Density and Thermal Expansion of Wrought Aluminum Alloys 7041, 7075 and 7095 by Gamma Ray Attenuation Method," J. Mod. Phys., 4(3), pp. 331–336.
- [35] Brar, N. S., Joshi, V. S., and Harris, B. W., 2009, "Constitutive Model Constants for Al7075-T651 and Al7075-T6," AIP Conference Proceedings, AIP, vol. 1195, no. 1, pp. 945–948.
- [36] Summers, P. T., Chen, Y., Rippe, C. M., Allen, B., Mouritz, A. P., Case, S. W., and Lattimer, B. Y., 2015, "Overview of Aluminum Alloy Mechanical Properties During and After Fires," Fire Sci. Rev., 4(1), p. 3.
  [37] Krishnan, K. N., 2002, "On the Formation of Onion Rings in Friction Stir Welds,"
- [37] Krishnan, K. N., 2002, "On the Formation of Onion Rings in Friction Stir Welds," Mater. Sci. Eng. A, 327(2), pp. 246–251.
- [38] Cole, E. G., Fehrenbacher, A., Duffie, N. A., Zinn, M. R., Pfefferkorn, F. E., and Ferrier, N. J., 2014, "Weld Temperature Effects During Friction Stir Welding of Dissimilar Aluminum Alloys 6061-t6 and 7075-t6," Int. J. Adv. Manuf. Technol., 71(1-4), pp. 643-652.
- [39] Fratini, L., Buffa, G., Palmeri, D., Hua, J., and Shivpuri, R., 2006, "Material Flow in FSW of AA7075–T6 Butt Joints: Numerical Simulations and Experimental Verifications," Sci. Technol. Weld. Join., 11(4), pp. 412–421.